3D Programmable Metamaterials Based on Reconfigurable Mechanism Modules

Weiqi Liu, Hanqing Jiang, and Yan Chen*

Mechanical metamaterials are of tremendous research interest due to their unconventional properties that arise from unit microstructure. Shape-reconfiguration is an effective method to realize programmability on various properties for different tasks of a structure or system, while existing researches focus on multiple degree-of-freedom (DOF) systems or limited configurations that morph along a single kinematic path. Here, starting from a one-DOF Wohlhart polyhedron module, its interesting topological transformation is explored along multiple motion paths through kinematic bifurcations, accompanied by tunable mechanical properties, including Poisson's ratio, chirality, and stiffness. Furthermore, these modules are tessellated into 3D metamaterials to harness their reconfigurability to independently program the Poisson's ratios in orthogonal planes within a wide range of negative Poisson's ratio, positive Poisson's ratio, and even zero Poisson's ratio. This work opens up avenues for the design of programmable metamaterials based on the perspective of kinematic bifurcation generating from single DOF systems, which can readily be applied in shape-morphing systems in various fields, such as flexible metamaterials, morphing architectures, and deployable structures.

1. Introduction

Mechanical metamaterials[1–3] are classified as artificially designed structures and exhibit intriguing and sometimes counterintuitive properties that cannot be achieved in natural materials, including negative or zero Poisson's ratio,[4–9] negative compressibility,[10–11] vanishing shear modulus,[12–13] negative thermal expansion,[14–15] etc. Generally, the mechanical properties of metamaterials are derived from the geometry and spatial tessellation of cell microstructure rather than material composition.[16] For example, a large number of 2D or 3D artificial negative Poisson's ratio structures have emerged, which are obtained by periodically assembling transformable elements via rotation, array, or mirror image, e.g., re-entrant structures,[17–21] chiral structures,[22–23] rotating units,[24–26] and origami units.[27–28] However, in most of the current researches, the unit cells in the metamaterial tessellation are of one type with identical deformation properties, which leads to the fact that the resultant metamaterials' characteristics are limited to a small range during the flexible deformation,[29–30] making it suitable only for a task with specific functional requirements. Therefore, it is critical to rationally design unit cells' microstructure and spatial arrangement to achieve reconfigurable properties for the multifunctional requirements.[31–32]

The programmability of metamaterials refers to the fact that the desired mechanical property is a function of controllable parameters, e.g., geometric parameters, boundary conditions, and external constraints.[33–37] Recently, the shape-reconfigurable system through structural instability or structural deformation has also been identified as an effective method to realize tunability and programmability in mechanical metamaterials. For example, mechanical properties, e.g., stress–strain curves or shapes, can be encoded by switching among different stable states of bistable or multistable modules.[38–40] In addition, origami-inspired designs that can fold along predefined creases have been widely used in metamaterials to achieve tunable and programmable properties, e.g., Poisson's ratio,[28,37] chirality,[41] or stiffness,[42] due to powerful continuous morphing ability. Of particular interest here are mechanism-based metamaterials with the capability of undergoing large shape morphing, where rigid elements are assembled and then acted as planar, spherical, or spatial mechanisms. On one hand, the characteristic of reliable deformation path is essential for tunable and programmable properties, which makes mechanism-based metamaterials widely used in designing the microstructure of metamaterials, particularly in rigid origami and kirigami inspired ones.[27–28,37,41,43–52] On the other hand, the deformation pattern of these mechanism-based metamaterials

W. Liu, Y. Chen
School of Mechanical Engineering
Tianjin University
Tianjin 300072, P. R. China
E-mail: yan_chen@tju.edu.cn
H. Jiang
School of Engineering
Westlake University
Hangzhou 310024, P. R. China
Y. Chen
Key Laboratory of Mechanism Theory and Equipment Design of
Ministry of Education
Tianjin University
Tianjin 300072, P. R. China

is similar to the zero-energy motions of the underlying mechanism.[53] Therefore, external forces easily excite deformation. However, the current works focus on programmable metamaterials that reconfigure along a single deformation path.[27–28,43–45] Efforts have also been made to investigate enhanced reconfigurable ones with multiple motion paths for programmable metamaterials including 3D reconfigurable architected materials,[49] transformable modular kirigami,[50] etc., yet it turns out to be typically multiple degree-of-freedoms (DOFs),[48–52] resulting in a challenging controllable deformation process.

Due to the lack of guidance from the underlying mechanism, the designs of reconfigurable metamaterial with multipathway but one DOF are rare. One of the methods to achieve reconfigurability is kinematic bifurcation,[54] which refers to the intersection point of multiple motion paths. Kinematic bifurcation differs from a multi-DOF system in that the former can only switch between its motion paths at the bifurcation point. Once it has passed through the point, the motion is determined by the selected path. Therefore, a single DOF system with kinematic bifurcation capabilities makes it an excellent candidate for designing reconfigurable metamaterials with programmable functionality, since they can be morphed into various configurations while also having a predefined and reliable path.

This paper proposes a one-DOF reconfigurable module with multiple predefined and reliable deformation paths. This construction module of the metamaterials can continuously bifurcate between expandable cube (EC) path, elongated prism (EP) path, and locked twist (LT) path through inherent kinematic bifurcation, accompanied by negative Poisson's ratio (NPR), positive Poisson's ratio (PPR), and zero Poisson's ratio (ZPR) behaviors as well as local and global chirality and tunable stiffness. Further, configurations of the module in EC and EP paths are used to construct 3D metamaterials yet without the frustration that impedes functionality due to compatible topological features. By regulating the proportion of modules in PPR or NPR states through reconfiguration, Poisson's ratios of metamaterials can be programmed independently in orthogonal planes within a wide range of NPR, PPR, and even ZPR for the first time. This work paves a new way to design programmable metamaterials through kinematic bifurcation.

2. Results

2.1. The Mechanism Module

We begin with the Wohlhart polyhedron[55] in **Figure 1**a, which acts as the mechanical basis of the module. First, the planar link group (PLG) is constructed with four identical rigid links of sides a and b attached to the square center body (side length $a \times a \times b$) through revolute (R) joints. The folding angle α determines the configuration of PLG by keeping rigid links rotationally symmetric and rotate about the center O clockwise or anticlockwise. Second, six identical clockwise rotation PLGs lying on faces of regular hexahedron are interconnected by R joints on the edges of cube connectors (side length b) to form a Wohlhart polyhedron, which is a highly overconstrained system with only one DOF working as an expandable cube.[55–56] Our focus here is on its reconfigurability and how to design programmable metamaterials with this mechanism as module.

The analysis on the kinematic characteristics of Wohlhart polyhedron reveals that there are three distinct motion paths, i.e., EC, EP, and LT paths, and two bifurcation points between EC and EP paths, EP and LT paths as shown in Figure 1b (Section S1 and Video S1, Supporting Information). Considering whether the rotation direction of each rotation PLG is clockwise or anticlockwise about coordinate axes, there are a total of 32 (=$2^6/2$, it is considered as one case when all the PLGs rotate in the opposition direction after passing B_0 if no bifurcation occurs) cases for EC path, i.e., EC_i^f–EC_i^p–B_0, where the subscript i (=1, ..., 32) represents the ith path, and superscript f and p represent fully folded and partially folded configurations, respectively. Meanwhile, EP path is divided into three cases (EP_x, EP_y, and EP_z) according to the orientation, and so is LT path (LT_x, LT_y, and LT_z). Configuration B_0 is one of the kinematic bifurcation points where this module can switch between EC and EP paths. Configurations B_x, B_y, and B_z, the folded state of the module in EP path as well as the unfolded state of the module in LT path, are also another type of bifurcation points, where the module can switch between EP and LT paths. Figure 1c demonstrates a complete motion process of the prototype from EC_1^f to LT_z^f, where parameters are selected as $a = 80$ mm, $b = 40$ mm (detailed fabrication in the Experimental Section, and Section S2 in the Supporting Information). Due to the similarity in three orthogonal directions, we only discuss the property in z-direction in the following analysis.

Apparently, the geometric dimensions of the module, i.e., the width (W), breadth (B), and height (H) in x, y, and z directions, have undergone significant changes during the motion process. The completed motion curves of this module with three paths are shown in **Figure 2**a. Here, we take the detailed path EC_1^p–B_0–EP_z^p–B_z–LT_z^p as an example to demonstrate the properties of the module. It can be observed that the module in EC path is expanded from a smaller cube to the largest size at B_0 then continuously folded up as the rotation angles in orthogonal planes increase with $\alpha = \beta = \gamma$.

The geometrical dimensions of the module in EC path are

$$W = B = H = a \sin\alpha + a \cos\alpha + a\sqrt{\sin 2\alpha} + 2b \tag{1}$$

in which $\alpha \in [0, \pi/2]$. Thus, its Poisson's ratios ν_{HB} and ν_{BW} are always –1 independent of geometric parameters (solid lines in Figure 2b) (Section S3, Supporting Information). Once the module reaches the bifurcation point B_0 ($\alpha = \beta = \gamma = \pi/4$), there are two possible paths, one is that the module is kept in the EC path as a cube to fold up with $\alpha = \beta = \gamma$ moving toward $\pi/2$ (red line in Figure 2a), the other one is that the module switches into EP path (blue line in Figure 2a) with PLGs on the four side faces shrink inward in a translational way. In this case

$$\beta = \gamma = \arcsin\left(\frac{\sin\alpha + \cos\alpha + \sqrt{2\sin\alpha\cos\alpha} - 1}{2}\right) \tag{2}$$

and

$$W = B = a + 2a\sin\beta + 2b \tag{3}$$
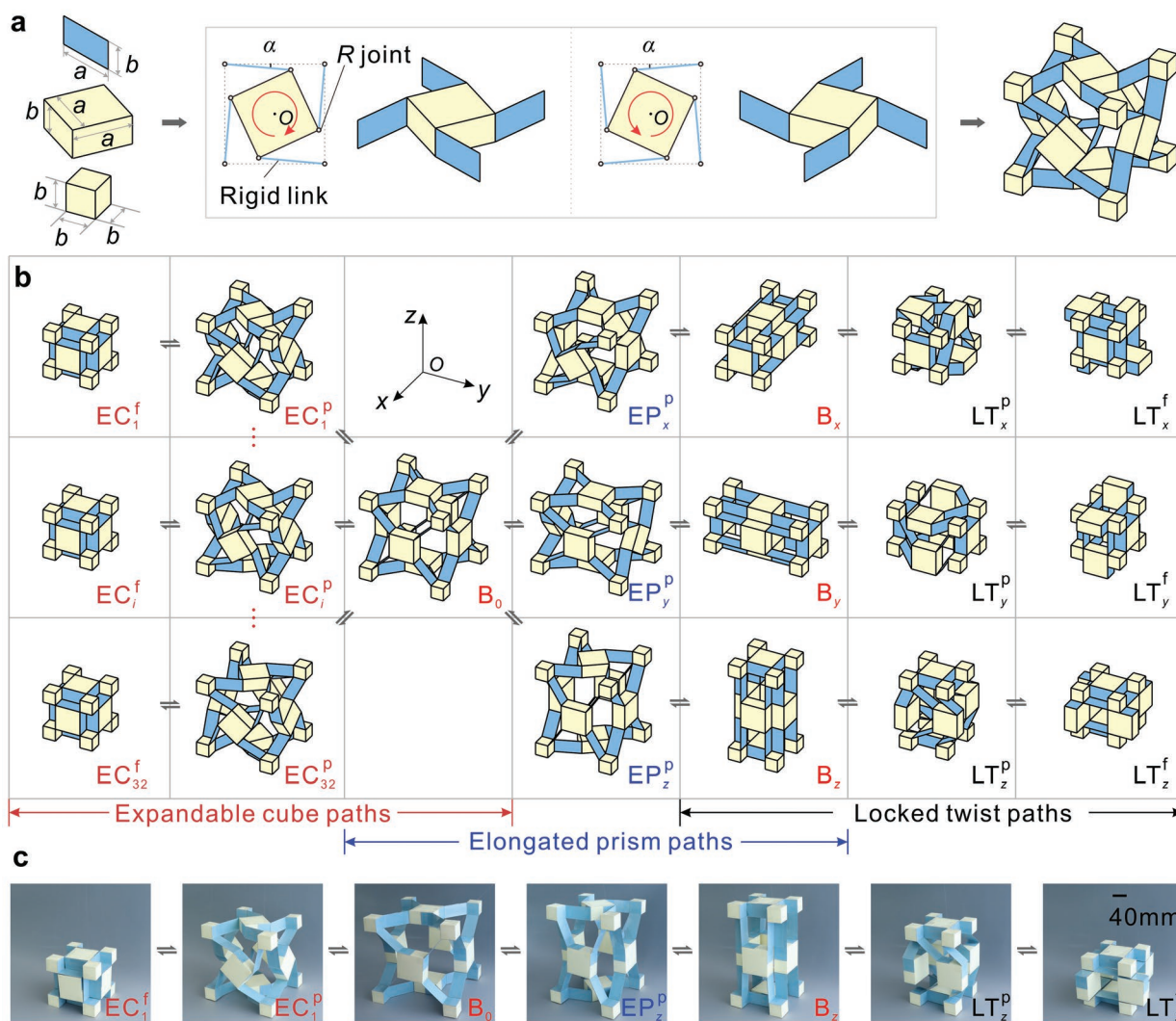
$$H = a + 2a\cos\beta + 2b \tag{4}$$

Figure 1. The mechanism basis of the module. a) The Wohlhart polyhedron is formed by connecting PLGs with cube connectors. The geometry of rigid link, square center body, and cube connector (left). Views of the clockwise rotation PLG and the anticlockwise rotation PLG (middle). Overview of the Wohlhart polyhedron (right). b) Kinematic bifurcation of the Wohlhart polyhedron. The motion paths of the module are divided into expandable cube path, elongated prism path, and locked twist path. B_0, B_x, B_y, and B_z are bifurcation configurations. c) The reciprocate process of the prototype from EC_1^f to LT_z^f with $a = 80$ mm and $b = 40$ mm.

in which $\beta \in [0, \pi/4]$.

It is evidently observed that the motion of the module in EP path is PPR behavior, and corresponding Poisson's ratios with $a/b = 2$ are illustrated in Figure 2c (solid lines). Theoretical results also suggest that the Poisson's ratios in EP path are insensitive to variations in geometrical parameters a/b (Section S3, Supporting Information). When $\beta = 0$ on the EP path, $\alpha = 0$ or $\pi/2$ depending on the rotation direction of PLGs on the top and bottom faces, the module reaches B_z bifurcation configuration, where the EP path is at limited end. Hence, the module can return on the EP path or bifurcate to the LT path with two rotation PLGs on top and bottom faces are locked at $\alpha = 0$ or $\pi/2$, and four PLGs on the side faces twist clockwise or anticlockwise about z-axis when $\beta = \gamma$. Here, the variation of geometric dimensions of the module in LT path is mainly divided into two

stages with $a/b > 1$ (Section S3, Supporting Information). When $\beta = \gamma \leq \arcsin(b/a)$, the projection of four PLGs on the side faces in the x–y plane is always within the projection of the rotation PLG ($\alpha = 0$ or $\pi/2$) on top and bottom faces, resulting in W and B remain constant $a+2b$. When the folding angle $\beta = \gamma > \arcsin(b/a)$, W and B become elongated simultaneously. Therefore, the geometrical dimensions of the module in LT_z path are

$$W = B = \begin{cases} a + 2b, & \text{if } \sin\beta \leq b/a \text{ or } a \leq b \\ a + 2a\sin\beta, & \text{if } \sin\beta > b/a \text{ and } a > b \end{cases} \quad (5)$$

and

$$H = a + 2b + 2a\cos\beta \quad (6)$$

**ADVANCED
SCIENCE NEWS**

www.advancedsciencenews.com

**ADVANCED
FUNCTIONAL
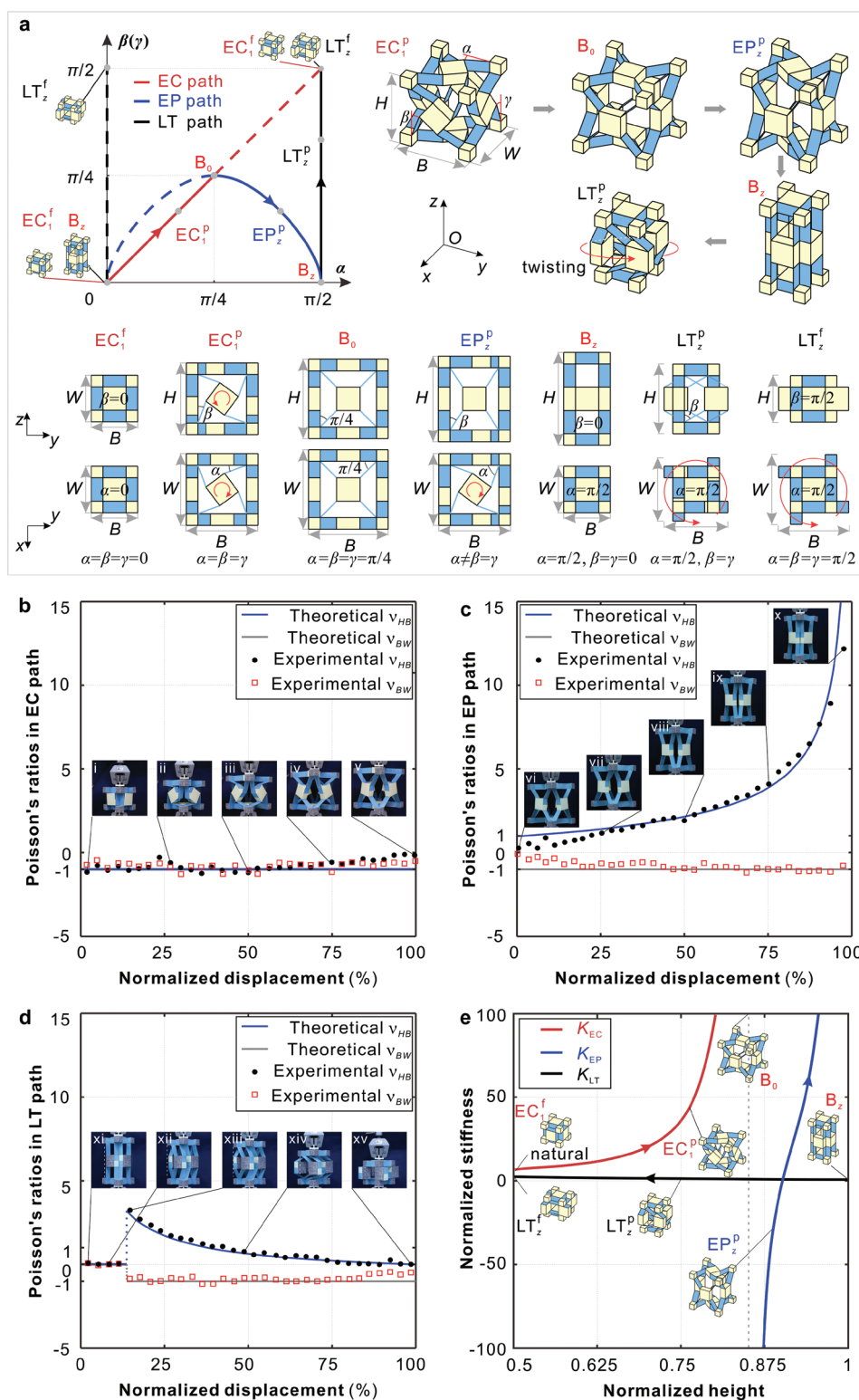MATERIALS**

www.afm-journal.de

Figure 2. Mechanical properties of a single module. a) The kinematic paths, and overall, front and top views of typical configurations. The variations of geometric dimensions of the module, the width (W), breadth (B), and height (H), in the x, y, and z directions are characterized by rotation angles α, β, and γ. Kinematic paths defined as angle relations during its reconfiguration in EC, EP, and LT paths. The module cannot switch into LT paths from the fully folded configuration in EC path at $\alpha = \beta = \gamma = 0$ or $\pi/2$, although there is an intersection point. The red arrow-arcs on PLGs and the module indicate the local and global chiralities, respectively, when the module switches between different paths. b–d) The theoretical and experimental Poisson's ratios of a module in EC, EP, and LT paths with $a/b = 2$, respectively. Black speckles on the specimen are used to measure the dimensions with a digital image correlation system (DIC). e) Stiffness K_i (i = EC, EP, and LT) of the module in different paths. The normalized height is expressed as H/H_{max}, where H_{max} is the maximum height of the module at configuration B_z.

in which $\beta \in [0, \pi/2]$.

Consequently, Poisson's ratios of the module in LT path with $a/b = 2$ is discontinuous as shown in Figure 2d (solid lines), i.e., Poisson's ratios v_{HB} and v_{BW} remain 0 first (ZPR mode), then v_{HB} suddenly increases to a positive value and then gradually decreases to 0 while v_{BW} suddenly drops to and remains at −1. We can further program this step point of Poisson's ratios by changing the geometrical parameters a/b (Section S3, Supporting Information). The interval of the ZPR mode lengthens as the value of a/b decreases, eventually reaching a full ZPR mode throughout the deformation process once $a/b \leq 1$.

The tension and compression experiments for a single module were then conducted to validate the aforementioned theoretical analysis (see the Experimental Section, and Section S4 in the Supporting Information). The recorded deformation process shows that W, B, and H of the module in EC path increase simultaneously during tension (i–v in Figure 2b) (Video S2, Supporting Information). Then, the specimen goes through another stage (vi–x in Figure 2c) after passing through the bifurcation configuration B_0, where W and B decrease while H increases continuously (Video S3, Supporting Information). After bifurcation point B_z, both W and B of the specimen in LT path are equal to $a+2b$ (xi–xii in Figure 2d) during compression, until the projection of rotation PLGs ($\alpha = 0$ or $\pi/2$) on the x–y plane cannot cover that of four PLGs on the side faces (xiii–xv in Figure 2d) (Video S4, Supporting Information). We find that the quantitative values of the experimental results are in good agreement with theoretical v_{HB} and v_{BW}, although results differ slightly at the 75–100% stage due to gravity.

From the experiments (Videos S2–S4, Supporting Information) and the red arrow-arcs marked in Figure 2a, we can tell that this module also exhibits distinct chirality property when moving along different kinematic paths. First, in the EC path, all six rotation PLGs on six faces rotate clockwise or anticlockwise independently to generate enhanced local chirality; second, in the EP path, only two rotation PLGs on two opposite faces normal to the elongated direction has the local chirality while the rest four have the translation with no chirality; third, in the LT path, two rotation PLGs on top and bottom faces are locked at $\alpha = 0$ or $\pi/2$, and four PLGs on the side faces twist clockwise or anticlockwise about z-axis when $\beta = \gamma$ to produce a global chirality. Based on the properties on the Poisson's ratios and chirality, we can also find that the reconfiguration of one module among three kinematic paths can be controlled through the relative displacements of the cube connectors or the combination of force or torque applied to the square central bodies at the bifurcated points (Section S5, Supporting Information). Additionally, the stiffness will also change significantly when the module is switched between different paths (Section S6, Supporting Information). We assume that each joint in the module is considered as a linear elastic spring hinge,[47] and fully folded configuration EC_1^f is the natural state of spring. To follow the movement path in Figure 2a, the stiffness of the module is shown in Figure 2e. The tension stiffness K_{EC} of the module in the EC path increases sharply as all spring joints move from 0 to $\pi/4$. At the bifurcation point B_0, the module deformation energy is at an unsmooth increasing state (nondifferentiable point) as some of the spring joints are further rotated as the others return toward the natural state,

resulting the force is discontinuous and the stiffness switches from $+\infty$ to $-\infty$ (Figure S11, Supporting Information). Subsequently, the stiffness K_{EP} in the EP path will undergo a change from negative to positive with the increase of deformation. Meanwhile, the bifurcation point B_z, is also a nondifferentiable point of system energy and the stiffness K_{LT} of the module in LT path increases at a lower level under compression as the joints on top and bottom faces are locked.

If tessellating the module through translation and array in 3D space, we obtain periodic metamaterials, whose properties are determined by the single module. The metamaterial will have the capability to continuously switch between NPR, PPR, and ZPR modes, relying on modules reconstructing between EC, EP, and LT paths (Section S7, Supporting Information). However, its programmability is still very limited as theoretical results (Section S3, Supporting Information) suggest that the Poisson's ratios in EC and EP paths are insensitive to variations in geometrical parameters a/b.

2.2. 3D Metamaterials with Programmable Properties

2.2.1. The Series Assembly with $(m_z + n_z)$ Modules

To enhance the programmability of metamaterials, we propose a combinatorial design strategy as shown in **Figure 3**a. Generally, under uniaxial tension F, PPR material tends to contract in the direction perpendicular to the applied load (Figure 3a left). In contrast, the NPR material elongates simultaneously along and perpendicular to the load directions when stretched. If the deformation of two neighboring units in the loading direction is consistent all the time, the two units can be stacked together in the direction perpendicular to the applied load. This combinational rule can also be extended to 3D PPR material and NPR materials (Figure 3a middle). Take two modules, one in PPR state on EP path, and one in NPR state on EC path (Figure 3a right). The dimensions of rotation PLGs are equal as long as their folding angle α is the same, which provides the possibility to connect two modules in EP and EC paths through the shared faces of four cube connectors (see orange lines in Figure 3a right). For ease of visualization, we use green right square prism and blue regular hexahedron with bumps and dents texture for connection to schematically represent the modules in PPR (state "1") and NPR (state "0") modes, respectively.

The series assembly with $(m_z + n_z)$ modules in Figure 3b is then constructed, of which m_z modules in PPR state and n_z modules in NPR state. Each module is equipped with the ability to switch between the state "1" and "0" through their inherent kinematic bifurcations (Figure 3b). Thus, this unique series assembly after fabrication is expected to be reconstructed into ones with arbitrary proportions and arrangement order of PPR and NPR modules. For example, if partial modules switch from the "1" state to the "0" state or vice versa without changing the total number of units ($m_{z1} + n_{z1} = m_{z2} + n_{z2} = m_{z3} + n_{z3}$), the proportion of NPR and PPR modules n_z/m_z changes. As m_z and n_z are any non-negative whole number, n_z/m_z could be any rational number within $[0, +\infty)$. The width W and breadth B of this series assembly are equal, so the value of Poisson's ratio v_{BW} is always −1 (Section S8, Supporting Information).
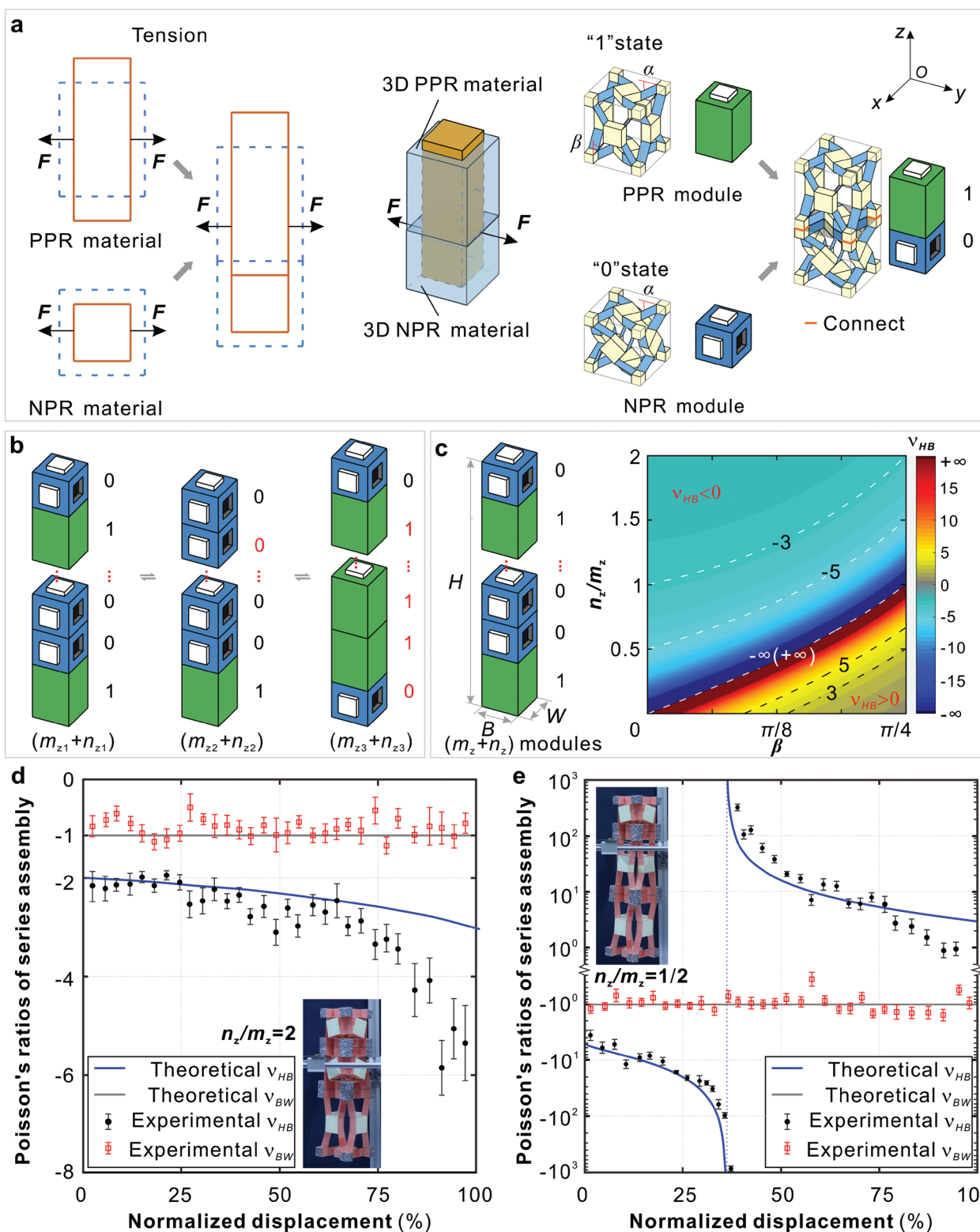
Figure 3. The series assembly with $(m_z + n_z)$ modules, with m_z modules in PPR state and n_z modules in NPR state. a) Schematic diagram of a two-module assembly with one in PPR state (marked as state "1") and one in NPR state (marked as state "0"). The modules in PPR and NPR states are represented schematically by the green right square prism and blue regular hexahedron with bumps and dents texture. b) Reconfiguration of module states to regulate n_z/m_z ($m_{z1} + n_{z1} = m_{z2} + n_{z2} = m_{z3} + n_{z3}$). c) A series assembly of m_z PPR and n_z NPR modules with $a/b = 2$ and its contour plot of Poisson's ratio ν_{HB}. d,e) Comparative plots of theoretical and experimental Poisson's ratios of three modules stacked in series with $n_z/m_z = 2$ and $n_z/m_z = 1/2$. Data are expressed as the mean and standard deviation of three measurements.

Its analytical contour plot indicates Poisson's ratio ν_{HB} (Equation (7)) of the series assembly with $a/b = 2$ cover the entire design space $(-\infty, +\infty)$ in Figure 3c as reconfiguration of module states is a rapid and effective way to regulate n_z/m_z. Specifically, ν_{HB} keeps negative during the whole folding motion if $n_z/m_z \geq 1$. Otherwise, ν_{HB} changes from a negative value to $-\infty$ with β increasing, then switches to $+\infty$ at $\beta = \arctan(n_z/m_z)$, and finally reaches a positive value. The series assembly with different values of n_z/m_z exhibits distinct but predictable mechanical properties, which provides a new paradigm for the programmability of Poisson's ratio.

$$\nu_{HB} = -\frac{\mathrm{d}B}{\mathrm{d}H} \times \frac{H}{B} = -\frac{am_z(1+2\cos\beta) + an_z(1+2\sin\beta) + 2b(m_z + n_z)}{(n_z - m_z\tan\beta)(a(1+2\sin\beta) + 2b)} \quad (7)$$

where $\beta \in [0, \pi/4]$ is the folding angle of the module in EP path.

Moreover, we conducted tension experiments with series assemblies ($n_z/m_z = 2$, $n_z/m_z = 1$, $n_z/m_z = 1/2$) in which modules are joined by a strong quick-drying glue (Videos S5–S7 and Section S9, Supporting Information). The results for three-module assembly with $n_z/m_z = 2$ in Figure 3d show that Poisson's ratio ν_{HB} remains negative and decreases with the deformation degree, while ν_{BW} fluctuates around -1. Then one of the PPR modules is reconstructed to NPR state to set $n_z/m_z = 1/2$ (Figure 3e). We observe the transition of ν_{HB} from -852.89 to 375.47, while ν_{BW} remains close to -1. Figure 3d,e shows that the natures and trends of mechanical response between theoretical and experimental results remain similar. But the difference of values ν_{HB} grows more prominent since the effect of gravity on deformation is more significant with the increase in the number of modules.

2.2.2. Metamaterials with the 3D Tessellation of Modules

The metamaterials can be further built in 3D space by tessellating multiple series assemblies. Two design schemes for 3D metamaterials are proposed as follows.

Scheme I: Identical series assemblies composed of m_z modules in PPR state and n_z modules in NPR state are parallelly and periodically tessellated (**Figure 4**a). There are i and j such columns in x and y directions, respectively. Each column's Poisson's ratios are identical. Therefore, the Poisson's ratios, of the whole metamaterial in Figure 4a, are the same as a single column, i.e., ν_{HB} can also be encoded by regulating the proportion of modules in PPR or NPR states according to Figure 3c, while ν_{BW} remains -1.

Scheme II: Series assemblies with $(m_x + n_x)$, $(m_y + n_y)$, and $(m_z + n_z)$ modules in x, y, and z directions, respectively, are implanted to form the frame of a cuboid tessellation (Figure 4b). Note that the corners are always NPR modules because its three common-point faces are used to connect other three modules simultaneously, i.e., $n_i \geq 2$ ($i = x, y, z$). Therefore, n_i/m_i could be any rational number within $[2/(2 + m_i), +\infty)$. The total number and proportion of modules in PPR or NPR states of series assemblies on parallel edges are identical, but the arrangement order of modules is not strictly limited.

In this case, Poisson's ratios ν_{HB} in the y–z plane and ν_{BW} in the x–y plane are (Section S10, Supporting Information)

$$\nu_{HB} = -\frac{\mathrm{d}B}{\mathrm{d}H} \times \frac{H}{B} = -\frac{(n_y - m_y\tan\beta)(am_z(1+2\cos\beta) + an_z(1+2\sin\beta) + 2b(m_z + n_z))}{(n_z - m_z\tan\beta)(am_y(1+2\cos\beta) + an_y(1+2\sin\beta) + 2b(m_y + n_y))} \quad (8)$$

and

$$\nu_{BW} = -\frac{\mathrm{d}W}{\mathrm{d}B} \times \frac{B}{W} = -\frac{(n_x - m_x\tan\beta)(am_y(1+2\cos\beta) + an_y(1+2\sin\beta) + 2b(m_y + n_y))}{(n_y - m_y\tan\beta)(am_x(1+2\cos\beta) + an_x(1+2\sin\beta) + 2b(m_x + n_x))} \quad (9)$$

where $\beta \in [0, \pi/4]$ is the folding angle of the module in EP path.

From Equations (8) and (9), we can tell that the Poisson's ratios of the 3D metamaterial in Figure 4b can be programmed by regulating the combination ratios of PPR and NPR states on EP and EC paths in three directions, n_i/m_i ($i = x, y, z$), independent as well as the folding angle β related to the configuration. First of all, let us fix $a/b = 2$ and $\beta = \pi/6$ to see the effect of n_i/m_i on the Poisson's ratios. For ν_{HB}, there are two boundaries (Figure 4c), i.e., $n_y/m_y = \tan\beta$ and $n_z/m_z = \tan\beta$, which are the transitions of ν_{BW} between negative and positive, and divide the design space $(-\infty, +\infty)$ into four regions. Poisson's ratio ν_{HB} can be encoded as any negative values once n_y/m_y and $n_z/m_z \in (0, \tan\beta)$, or n_z/m_z and $n_z/m_z \in (\tan\beta, +\infty)$. Otherwise, ν_{HB} is positive. Apparently, n_x/m_x and n_y/m_y play the same role in the programming of ν_{BW} (see Figure 4d). Moreover, n_z/m_z and n_x/m_x are independent variables of ν_{HB} and ν_{BW} as characterized in Equations (8) and (9), implying that Poisson's ratios ν_{HB} and ν_{BW} can be programmed independently. Meanwhile, similar as the single module and series assemblies, the Poisson's ratios of the whole metamaterial can be tuned by configurations described by folding angle β, and they are not insensitive to variations in geometrical parameters a/b (Section S10, Supporting Information).

To demonstrate the programming on the characteristics of metamaterials' Poisson's ratios, let us take an example with $(m_x + n_x = 6)$, $(m_y + n_y = 5)$, $(m_z + n_z = 8)$ modules and $a/b = 2$ (Figure 4e). Every module except those eight on the cuboid corners can switch between the PPR and NPR states on EP and EC paths. Hence, there are totally 140 modes with distinct characteristics of Poisson's ratios. In the extremal mode that all the modules in the tessellation are in NPR state, the metamaterial will be of 3D negative Poisson's ratios with $\nu_{HB} = \nu_{BW} = -1$. Let us take a random mode with $n_x/m_x = 2$, $n_y/m_y = 3/2$, and $n_z/m_z = 1$ (Figure 4e, mode I), the metamaterial is with 3D negative Poisson's ratios as both ν_{HB} and ν_{BW} decrease monotonically in negative values due to $n_i/m_i \geq 1$ (blue solid lines in Figure 4f,g). Then, two NPR modules in each x-direction series assembly are reconfigured to PPR state to set $n_x/m_x = 1/2$ while keeping $n_y/m_y = 3/2$, $n_z/m_z = 1$ (mode II). It is observed that ν_{HB} is the same as that of mode I (the gray dashed line coincides with the blue solid line in Figure 4f), while ν_{BW} changes from negative to positive passing zero with the increasing folding angle β (gray dashed line in Figure 4g). Next, one NPR module in each y-direction series assembly is reconfigured
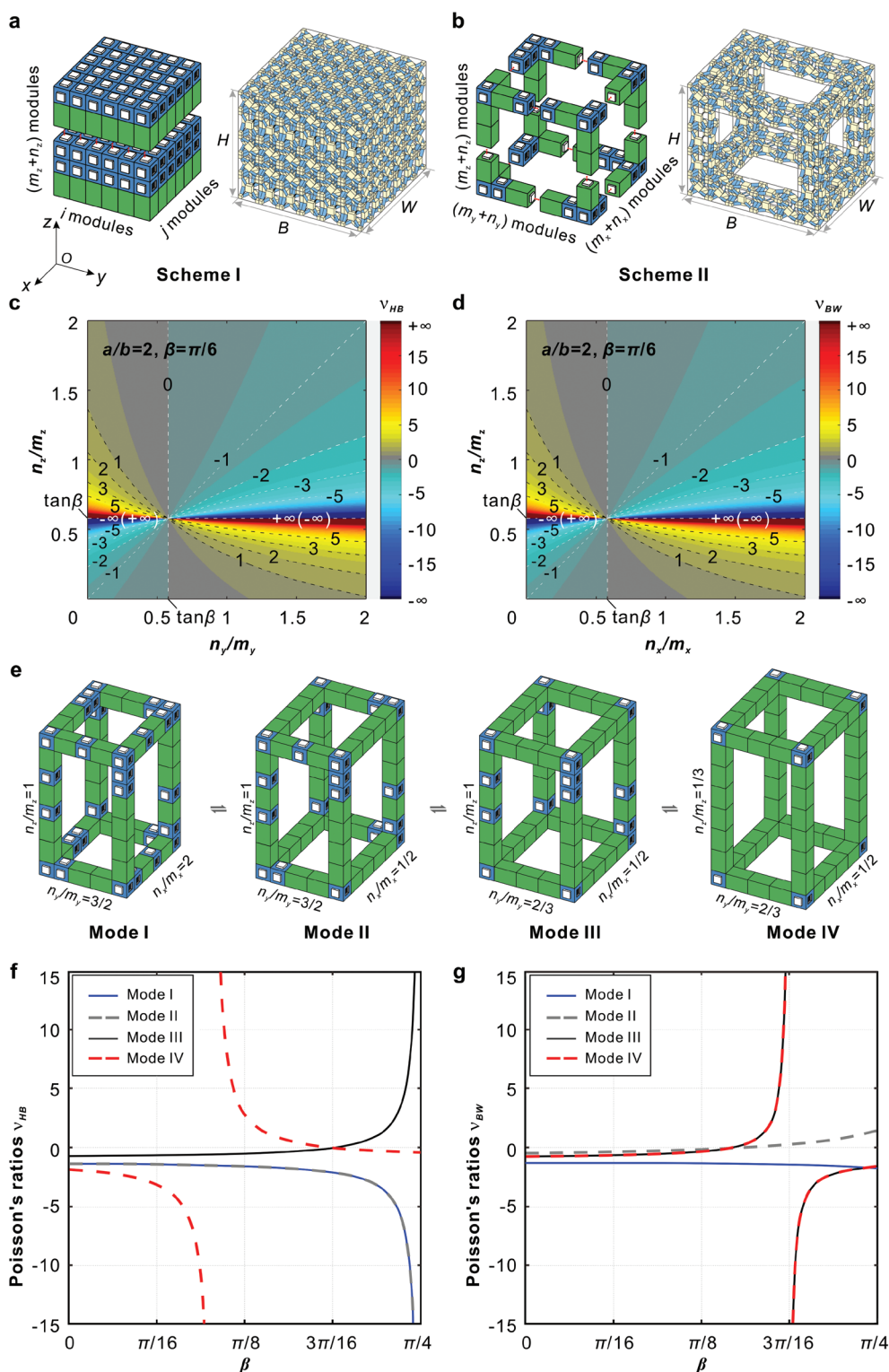
Figure 4. Metamaterials with the 3D tessellation of mechanism modules. a) Design scheme I of 3D metamaterials created by tessellating series assemblies in 3D space. Each column consists of $(m_z + n_z)$ modules. There are i and j such columns in x and y directions, respectively. b) Design scheme II of 3D metamaterials with $(m_x + n_x)$, $(m_y + n_y)$, and $(m_z + n_z)$ modules in x, y, and z directions, respectively, to form the frame of a cubic tessellation. c,d) The contour plots of ν_{HB} and ν_{BW} for 3D metamaterials in scheme II as function of n_i/m_i ($i = x, y, z$) when $a/b = 2$ and $\beta = \pi/6$. e–g) The reconstruction of the metamaterial with $(m_x + n_x = 6)$, $(m_y + n_y = 5)$, and $(m_z + n_z = 8)$ modules ($a/b = 2$) through bifurcation in four typical modes and the corresponding Poisson's ratios ν_{HB} and ν_{BW}, where $n_x/m_x = 2$, $n_y/m_y = 3/2$, and $n_z/m_z = 1$ in mode I, $n_x/m_x = 1/2$, $n_y/m_y = 3/2$, and $n_z/m_z = 1$ in mode II, $n_x/m_x = 1/2$, $n_y/m_y = 2/3$, and $n_z/m_z = 1$ in mode III, and $n_x/m_x = 1/2$, $n_y/m_y = 2/3$, and $n_z/m_z = 1/3$ in mode IV.

**ADVANCED
SCIENCE NEWS**
www.advancedsciencenews.com

**ADVANCED
FUNCTIONAL
MATERIALS**
www.afm-journal.de

to PPR state to set $n_y/m_y = 2/3$ while keeping $n_x/m_x = 1/2$, $n_z/m_z = 1$ (mode III), both ν_{HB} and ν_{BW} have experienced significant changes due to the change of n_y/m_y. It is noted that ν_{HB} increases from –0.71 to +∞ with β, while ν_{BW} first increases from –0.78 to +∞, then switches to –∞ at $\beta = 33.69°$, and finally reaches –1.63 (black solid lines Figure 4f,g). Furthermore, if we set $n_z/m_z = 1/3$ by reconfiguring two NPR modules to PPR state and keep $n_x/m_x = 1/2$, $n_y/m_y = 2/3$, ν_{HB} will decrease from –1.86 to –∞, and then switches to +∞ at $\beta = 18.42°$, and finally reaches –0.41 (red dashed line Figure 4f) due to the change of n_z/m_z compared to mode III, while the value of ν_{BW} is the same with that in mode III as Poisson's ratio ν_{BW} is independent of n_z/m_z (the red dashed line coincides with the black solid line in Figure 4g). These four modes present the typical characteristics of 3D Poisson's ratios, i.e., both in-plane and out-plane negative ratios, one negative and one positive, or switching between the negative and positive several times during the deformation of metamaterials.

3. Conclusions

In this paper, by analyzing the kinematics of the Wohlhart polyhedron, we have revealed that this mechanism has three kinematic paths, EC, EP, and LT paths, interesting at bifurcation points, B_0 and $B_x/B_y/B_z$. Taking a single mechanism as the module, it can switch among distinct Poisson's ratios, NPR, PPR, and ZPR under the EC, EP, and LT paths through the bifurcation. Hence, Poisson's ratios can be tuned with the motion of module but are not sensitive to the geometric parameters. Such module also exhibits tunable chirality and stiffness along the different motion paths. Further studies found that modules in EC path with NPR state and that in EP path with PPR state can deform cooperatively due to compatible topological features, which provides a new paradigm to form a series assembly of the module, whose Poisson's ratios can be programmed by regulating the proportion of modules in PPR or NPR states through the reconfiguration of each module between NPR and PPR states. Next taking this series assembly as column, 3D metamaterials can be constructed by implanting the columns as the frame of a cuboid tessellation. Owing to the reconfigurability of the module, we can independently program the Poisson's ratios in orthogonal planes within a wide range from –∞ to +∞ by adjusting the ratio of the number of modules in PPR and NPR states, which greatly enhances the flexibility in the design of 3D metamaterials with programmable Poisson's ratios.

Mechanism-based metamaterials have shown great potential and advantages in the design of metamaterials with various advanced properties.[50–51] This design strategy can be extended to other reconfigurable mechanisms to design metamaterials, especially those combining different types of modules.[31] The reconfiguration of the module, accompanied by programmable properties, enables 3D metamaterials to be transformed into various deformation modes without disassembly and reassembly, providing the possibility to adapt to multiple environments and tasks. To achieve reconfigurability of metamaterials with a large number of modules, we can rely on certain materials, which can produce deformation responses based on external environmental stimuli such as magnetic, electric, light, or thermal fields, to synchronously drive modules at the

bifurcated states. Meanwhile, in the kinematics of mechanism, the focus is on the topology and the relative geometric condition, thus mechanism-based metamaterials are generally scale free. Their detailed scale is decided by both the request from the specific applications, as well as the manufacture process.

The metamaterials with switchable Poisson's ratio, local and global chirality and tunable stiffness in a wider tunable range are of great application potentials in shape-morphing systems for various fields, such as flexible metamaterials, morphing architectures, robotics, bioengineering tissue,[57] and deployable structures with both length and volume expansions.

4. Experimental Section

Fabrication of a Single Module: Cardboard was used to fold the center body (80 × 80 × 40 mm) and cube connector (40 × 40 × 40 mm) (Figure S6, Supporting Information). The blue or pink cardboard strip (160 × 40 × 40 mm) had two incisions for joints. Before using glue to connect the center body, the connector, and the cardboard strip, a layer of polyethylene terephthalate (PET) (80 × 40 × 0.4 mm) was needed to be pasted in the middle of the cardboard strip to improve the stiffness of the link. First, each PLG was constructed with four identical rigid links attached to the square center body. Then, PLGs were interconnected to the edges of cube connectors to form a module.

Measurement of the Mechanical Properties of a Single Module: A tension and compression experiment for a single module was conducted (Videos S2–S4 and Section S4, Supporting Information) on a vertical testing machine (Instron 5982). The specimen was tensioned (compression) with 160 mm displacement and a 0.5 mm s⁻¹ loading rate. The deformation process was captured by a CSI Vic-3D9M digital image correlation (DIC) system with a camera resolution of 2704 × 3384 pixels and a frame period of 500 ms.

Measurement of the Mechanical Properties of Series Assemblies: Horizontal tension experiments were conducted with series assemblies ($n_z/m_z = 2$, $n_z/m_z = 1$, $n_z/m_z = 1/2$) in which modules were joined by a strong quick-drying glue (Videos S5–S7 and Section S9, Supporting Information). The specimens were suspended in the diagonal direction on a fixed frame. One end of the specimen was directly glued on the frame, and the other end was fixed on the slider located on the frame. The slider was connected with the fixture of the displacement control system by Kevlar ROPE tows ($\varphi = 0.3$ mm). The specimen was then tensioned with 160 mm displacement and a loading rate of 0.5 mm s⁻¹. The deformation process was captured by the same DIC system with a camera resolution of 2704 × 3384 pixels and a frame period of 500 ms.

Supporting Information

Supporting Information is available from the Wiley Online Library or from the author.

Conflict of Interest

The authors declare no conflict of interest.

**ADVANCED
SCIENCE NEWS**

www.advancedsciencenews.com

**ADVANCED
FUNCTIONAL
MATERIALS**

www.afm-journal.de

Data Availability Statement

The data that support the findings of this study are available in the Supporting Information of this article.

[1] N. I. Zheludev, *Science* **2010**, *328*, 582.
[2] K. Bertoldi, V. Vitelli, J. Christensen, M. Van Hecke, *Nat. Rev. Mater.* **2017**, *2*, 17066.
[3] J. U. Surjadi, L. Gao, H. Du, X. Li, X. Xiong, N. X. Fang, Y. Lu, *Adv. Eng. Mater.* **2019**, *21*, 1800864.
[4] R. Lakes, *Science* **1987**, *235*, 1038.
[5] D. Prall, R. Lakes, *Int. J. Mech. Sci.* **1997**, *39*, 305.
[6] C. S. Ha, M. E. Plesha, R. S. Lakes, *Phys. Status Solidi B* **2016**, *253*, 1243.
[7] H. Park, H. Kwon, Y. An, W. R. Yu, M. W. Moon, K. Hur, *Phys. Status Solidi RRL* **2018**, *12*, 1800040.
[8] P. Soman, D. Y. Fozdar, J. W. Lee, A. Phadke, S. Varghese, S. Chen, *Soft Matter* **2012**, *8*, 4946.
[9] X. Chen, M.-H. Fu, W.-H. Li, S. V. Sheshenin, *Adv. Eng. Mater.* **2021**, *23*, 2001491.
[10] R. Gatt, J. N. Grima, *Phys. Status Solidi RRL* **2008**, *2*, 236.
[11] Z. G. Nicolaou, A. E. Motter, *Nat. Mater.* **2012**, *11*, 608.
[12] M. Wyart, H. Liang, A. Kabla, L. Mahadevan, *Phys. Rev. Lett.* **2008**, *101*, 215501.
[13] T. Bückmann, M. Thiel, M. Kadic, R. Schittny, M. Wegener, *Nat. Commun.* **2014**, *5*, 4130.
[14] R. Lakes, *J. Mater. Sci. Lett.* **1996**, *15*, 475.
[15] X. Guo, X. Ni, J. Li, H. Zhang, F. Zhang, H. Yu, J. Wu, Y. Bai, H. Lei, Y. Huang, *Adv. Mater.* **2020**, *33*, 2004919.
[16] M. Kadic, G. W. Milton, M. van Hecke, M. Wegener, *Nat. Rev. Phys.* **2019**, *1*, 198.
[17] I. Masters, K. Evans, *Compos. Struct.* **1996**, *35*, 403.
[18] U. D. Larsen, O. Signund, S. Bouwsta, *J. Microelectromech. Syst.* **1997**, *6*, 99.
[19] J. N. Grima, R. Gatt, A. Alderson, K. Evans, *Mol. Simul.* **2005**, *31*, 925.
[20] S. Hengsbach, A. D. Lantada, *Smart Mater. Struct.* **2014**, *23*, 085033.
[21] H. Yasuda, J. Yang, *Phys. Rev. Lett.* **2015**, *114*, 185502.
[22] A. Spadoni, M. Ruzzene, *J. Mech. Phys. Solids* **2012**, *60*, 156.
[23] M.-H. Fu, B.-B. Zheng, W.-H. Li, *Compos. Struct.* **2017**, *176*, 442.
[24] J. N. Grima, K. E. Evans, *J. Mater. Sci. Lett.* **2000**, *19*, 1563.
[25] J. N. Grima, K. E. Evans, *J. Mater. Sci.* **2006**, *41*, 3193.
[26] J. N. Grima, P. S. Farrugia, R. Gatt, D. Attard, *Phys. Status Solidi B* **2008**, *245*, 521.
[27] R. Peng, J. Ma, Y. Chen, *Mech. Mach. Theory* **2018**, *128*, 461.
[28] M. Schenk, S. D. Guest, *Proc. Natl. Acad. Sci. USA* **2013**, *110*, 3276.
[29] C. Coulais, E. Teomy, K. De Reus, Y. Shokef, M. Van Hecke, *Nature* **2016**, *535*, 529.
[30] X. Xin, L. Liu, Y. Liu, J. Leng, *Adv. Funct. Mater.* **2020**, *30*, 2004226.
[31] P. Jiao, A. H. Alavi, *Int. Mater. Rev.* **2020**, *66*, 365.
[32] X. Ren, R. Das, P. Tran, T. D. Ngo, Y. M. Xie, *Smart Mater. Struct.* **2018**, *27*, 023001.
[33] N. An, A. G. Domel, J. Zhou, A. Rafsanjani, K. Bertoldi, *Adv. Funct. Mater.* **2020**, *30*, 1906711.
[34] T. Chen, M. Pauly, P. M. Reis, *Nature* **2021**, *589*, 386.
[35] J. L. Silverberg, A. A. Evans, L. McLeod, R. C. Hayward, T. Hull, C. D. Santangelo, I. Cohen, *Science* **2014**, *345*, 647.
[36] J. N. Grima-Cornish, R. Cauchi, D. Attard, R. Gatt, J. N. Grima, *Phys. Status Solidi B* **2020**, *257*, 1900707.
[37] H. Wang, D. Zhao, Y. Jin, M. Wang, T. Mukhopadhyay, Z. You, *Appl. Mater. Today* **2020**, *20*, 100715.
[38] B. Haghpanah, L. Salari-Sharif, P. Pourrajab, J. Hopkins, L. Valdevit, *Adv. Mater.* **2016**, *28*, 7915.
[39] K. Liu, T. Tachi, G. H. Paulino, *Nat. Commun.* **2019**, *10*, 4238.
[40] N. Yang, C.-W. Chen, J. Yang, J. L. Silverberg, *Mater. Des.* **2020**, *196*, 109143.
[41] H. Feng, W. Lv, J. Ma, W. Chang, Y. Chen, J. Wang, *Appl. Phys. Lett.* **2020**, *116*, 194102.
[42] H. Fang, S. C. A. Chu, Y. Xia, K. W. Wang, *Adv. Mater.* **2018**, *30*, 1706311.
[43] M. Eidini, G. H. Paulino, *Sci. Adv.* **2015**, *1*, e1500224.
[44] S. A. Nauroze, L. S. Novelino, M. M. Tentzeris, G. H. Paulino, *Proc. Natl. Acad. Sci. USA* **2018**, *115*, 13210.
[45] E. T. Filipov, T. Tachi, G. H. Paulino, *Proc. Natl. Acad. Sci. USA* **2015**, *112*, 12321.
[46] Z. Wang, L. Jing, K. Yao, Y. Yang, B. Zheng, C. M. Soukoulis, H. Chen, Y. Liu, *Adv. Mater.* **2017**, *29*, 1700412.
[47] P. P. Pratapa, K. Liu, G. H. Paulino, *Phys. Rev. Lett.* **2019**, *122*, 155501.
[48] Y. Tang, Y. Li, Y. Hong, S. Yang, J. Yin, *Proc. Natl. Acad. Sci. USA* **2019**, *116*, 26407.
[49] J. T. Overvelde, T. A. De Jong, Y. Shevchenko, S. A. Becerra, G. M. Whitesides, J. C. Weaver, C. Hoberman, K. Bertoldi, *Nat. Commun.* **2016**, *7*, 10929.
[50] Y. Li, J. Yin, *Mater. Today Phys.* **2021**, *21*, 100511.
[51] Y. Li, Q. Zhang, Y. Hong, J. Yin, *Adv. Funct. Mater.* **2021**, *31*, 2105641.
[52] J. T. Overvelde, J. C. Weaver, C. Hoberman, K. Bertoldi, *Nature* **2017**, *541*, 347.
[53] N. Singh, M. van Hecke, *Phys. Rev. Lett.* **2021**, *126*, 248002.
[54] C. Song, Y. Chen, I.-M. Chen, *Mech. Mach. Theory* **2013**, *70*, 278.
[55] K. Wohlhart, presented at Proc. of the 2nd Workshop on Computational Kinematics, Seoul, May **2001**.
[56] H. Xiu, K. Wang, G. Wei, L. Ren, J. Dai, *J. Mech. Eng. Sci.* **2020**, *234*, 241.
[57] X. Yu, J. Zhou, H. Liang, Z. Jiang, L. Wu, *Prog. Mater. Sci.* **2018**, *94*, 114.